Journal of Power Sources 196 (2011) 10401–10414

Contents lists available at ScienceDirect

Journal of Power Sources

journal homepage: www.elsevier.com/locate/jpowsour

Optimal shifting of Photovoltaic and load fluctuations from fuel cell and electrolyzer to lead acid battery in a Photovoltaic/hydrogen standalone power system for improved performance and life time

S.G. Tesfahunegn[a,b,*], Ø. Ulleberg[a], P.J.S. Vie[a], T.M. Undeland[b]

[a] Institute for Energy Technology, NO-2027, Kjeller, Norway
[b] Norwegian University of Science and Technology, Trondheim, Norway

ARTICLE INFO

Article history:
Received 26 April 2011
Received in revised form 26 May 2011
Accepted 3 June 2011
Available online 15 June 2011

Keywords:
Battery
Cycle life
Electrolyzer
Fuel cell
PV
Smoothing

ABSTRACT

Cost reduction is very critical in the pursuit of realizing more competitive clean and sustainable energy systems. In line with this goal a control method that enables minimization of the cost associated with performance and life time degradation of fuel cell and electrolyzer, and cost of battery replacement in PV/hydrogen standalone power systems is developed. The method uses the advantage of existing peak shaving battery to suppress short-term PV and load fluctuations while reducing impact on the cycle life of the battery itself. This is realized by diverting short-term cyclic charge/discharge events induced by PV/load power fluctuations to the upper band of the battery state of charge regime while operating the fuel cell and electrolyzer systems along stable (smooth) power curves. Comparative studies of the developed method with two other reference cases demonstrate that the proposed method fares better with respect to defined performance indices as fluctuation suppression rate and mean state of charge. Modeling of power electronics and design of controllers used in the study are also briefly discussed in Appendix A.

1. Introduction

Fuel cells are considered potentially suitable as solar power backup particularly in remote area power systems such as those used to power telecom loads. Compared to diesel/steam generators, fuel cells boast higher efficiency, better reliability and faster load following capability. They are also very clean as they produce ultra-low emissions. Unlike diesel/steam generators whose fuel efficiency falls drastically at low power output, the efficiency of fuel cells stays almost unchanged down to 40% of rated power [1,2]. Much less maintenance requirement combined with very high power density of fuel cell systems makes them more suitable in remote places where frequent visits are difficult.

The use of peak-shaving battery storage together with fuel cell and water electrolyzer increases their capacity factor. This allows a reduction in investment cost of the fuel cell and electrolyzer systems as both can be sized to meet only the average load demand while the battery storage is used to shave shorter transitory peaks that may arise due to load power exceeding the combined power of PV and fuel cell. In an autonomous system having an integrated electrolyzer, using hydrogen (fuel cell and electrolyzer) as long term energy storage and a modestly sized battery as short term storage is therefore very advantageous. In this case, hydrogen is produced from excess solar energy during off-peak periods and is subsequently used by the fuel cell to generate electricity during peak load periods and low solar insolation hours.

In addition to the daily solar cycle, changing weather conditions and passing cloud cover lead to unstable power generation from PV systems. The latter may cause large, rapid power fluctuations which can reach ramp rates as high as 10%/min of installed PV capacity [3]. This may, therefore, mean the fuel cell and electrolyzer systems should follow these changes in addition to load variations. For example, even under constant load conditions, a fast increase in PV power would lead to a decrease in fuel cell power by the same amount and rate to save fuel while a decrease in PV power will have the opposite effect. Exposure of the fuel cell and electrolyzer to such short term and highly variable power conditions may lead to degradation of performance and life time, two important cost factors. Particularly, thermal management becomes a huge challenge due to the long thermal time constants involved forcing the fuel cell and electrolyzer systems to be operated at suboptimal temperature ranges [4,5]. In addition to performance degradation due to efficiency loss at temperatures outside nominal range, durability degradation may also occur due to temperature overshoot above limiting values and gas starvation of electrodes. To make

* Corresponding author at: Institute for Energy Technology, NO-2027, Kjeller, Norway. Tel.: +47 63806000.
E-mail address: Samson.gebre@ife.no (S.G. Tesfahunegn).

0378-7753/$ – see front matter © 2011 Elsevier B.V. All rights reserved.
doi:10.1016/j.jpowsour.2011.06.037

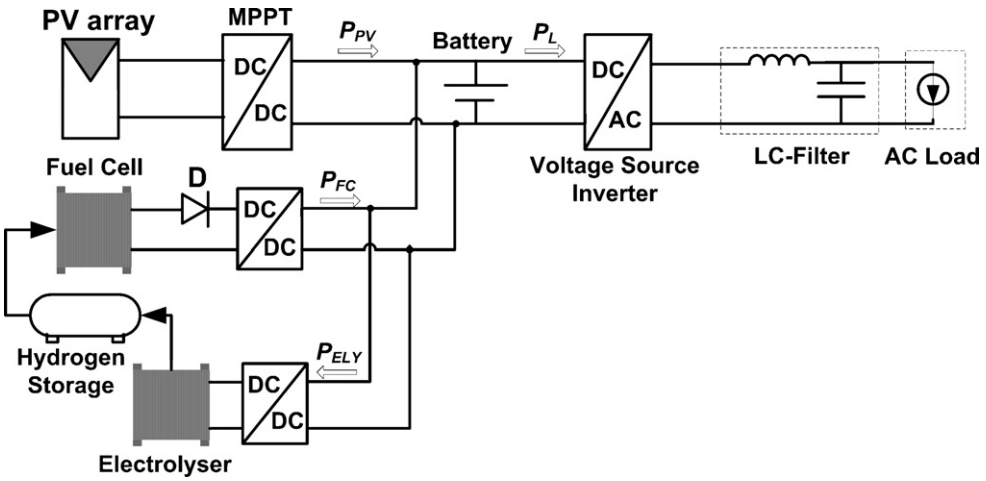

Fig. 1. Studied PV–hydrogen hybrid power system.

solar–hydrogen power systems economically competitive, the cost associated with performance and life time degradation should be reduced.

One way to alleviate the problem of operating the fuel cell and electrolyzer under highly variable power conditions is to use cheaper battery storage systems such as lead acid to absorb short term PV power fluctuations and load variations. However, in doing so, one may risk increased battery cycling which in turn reduces battery cycle life. Several stress factors lead to risk for aging mechanisms in lead acid batteries. In [6,7], the stress factors are identified and a benchmarking process is developed to help categorize renewable energy systems (RES) based on conditions of similar use of battery. Each category of RES is thus assigned a given set of intensity levels corresponding to each stress factor. To increase the cycle life of lead acid battery, the risks associated with the stress factors should be prevented or reduced. Sound battery management strategies and/or choice of the right type of lead acid battery can help decrease risk of aging. Though operating a battery under the most favorable operating regimes by using smart energy and power management strategies has great potential to improve cycle life, more expensive ways such as using oversized battery capacities have been used to achieve the same goal. To date only very few research efforts have been done to develop smart battery management methods that help prolong battery life (e.g. [8]) by operating them under optimal operating regimes.

In this article a control method which uses the advantage of an existing peak shaving battery to suppress short term power fluctuations with reduced impact on cycle life of the battery is presented. The method enables lead acid battery operating regimes that reduce the impact of stress factors such as operating at low state of charge (SOC), partial cycling and long periods between full charges. The premise of the method is cycling a battery at low SOC and long periods at low SOC and long time between full charge will accelerate aging of lead acid battery through high stratification and irreversible sulphation [7]. Refs. [9,10] present a life time model of lead acid battery including how SOC cycles starting at partial state of charge affect the cycle life. The method developed here enables to operate the fuel cell and electrolyzer along smooth power curves and diverts short term power fluctuations to the upper band of the battery SOC regime with possibilities of frequent recharge.

2. System description

The system used to study the developed control method is the common DC-bus architecture shown in Fig. 1 although the same will equally apply for AC-coupled systems as well. As the control method is pertinent to the DC-side of the system, it will also be valid for DC systems such as telecom loads. In the latter case, the voltage source inverter (VSI) and the Ac load will be replaced by a DC-load. In the system considered here lead acid battery is used as the short term storage and forms the common DC-bus voltage to which all other subsystems are connected. A single phase voltage source inverter (VSI) acts as the grid forming unit and converts the DC voltage to a high quality AC load voltage. In addition to reducing the total harmonic distortion (THD) in the load voltage, the LC-filter also helps to improve inverter power factor by producing some of the reactive power demand (in the filter capacitor). To maximize the PV output, a maximum power point tracker (MPPT) is used between the PV array and the DC-bus. Both the fuel cell and the electrolyzer are interfaced to the common DC-bus using DC/DC converters to adapt their voltage levels and enable active control of power flow. A storage tank stores the hydrogen generated by the electrolyzer during off-peak hours which is eventually re-electrified by the fuel cell during peak load hours. A step up transformer (not shown in figure) is also used to boost the inverter voltage to 230 V ac, 50 Hz. The turns ratio of the transformer is chosen based on the minimum inverter voltage (whose peak is equal to the minimum battery voltage $V_{batt,\min}$), voltage drops in filter and transformer V_{drop}, RMS of fundamental AC load voltage $V_{L,rms}$ and modulation index m_a. Assuming linear modulation, the voltage transformation ratio can be calculated as

$$n = \frac{N_s}{N_p} = \frac{V_{L,rms}\sqrt{2}}{m_a \times V_{Batt,\min} - V_{drop}} \quad (1)$$

where N_P and N_s are primary and secondary turns of the transformer, respectively. All system data and parameters can be found in Table 2.

3. Load smoothing using moving average

Assuming PV generation as negative load, the net load presented to the fuel cell and electrolyzer can be written as

$$P_{netL} = P_L - P_{PV} \quad (2)$$

where P_L and P_{PV} are the actual load and PV powers, respectively. The fluctuations in the net load P_{netL} will be function of variations in both P_{PV} and P_L. To suppress short term power fluctuations seen by the fuel cell and electrolyzer, the moving average of P_{netL} (3) can be used as the control power set point instead of the net load itself.

$$P_m = \frac{1}{T}\int_{t-T}^{t} P_{netL}\,dt \quad (3)$$

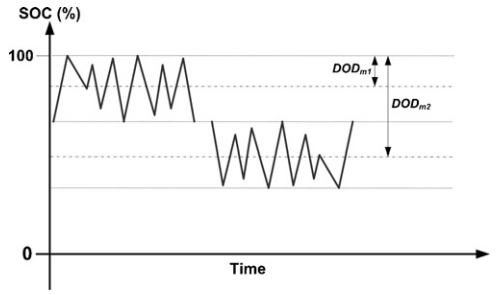

Fig. 2. Illustration of SOC swing for two different DOD_m points.

Battery storage is then used to compensate the differential power in (4) where P_{Batt} is the battery power and is here assumed positive during discharge. The choice of the averaging interval T depends on the level of suppression required and how much battery capacity can be allocated to do this. With a moving window of T, the power smoothing mechanism will enable to suppress all power variations having frequencies greater than $1/T$. This means if P_{netL} stays constant for T units or more, the smoothed power P_m will eventually attain the same value as P_{netL} and P_{Batt} becomes zero.

$$P_{Batt} = P_{netL} - P_m \tag{4}$$

A positive P_m implies that there is net power demand not met by the PV alone and therefore the fuel cell is operated where as a negative P_m means there is surplus PV power and therefore the electrolyzer is operated. In either case P_m acts as a reference to determine the power output and input respectively of the fuel cell and electrolyzer.

4. Mode switching control method

Short term fluctuations in PV output generally tend to have cyclic pattern with fast dips and subsequent surges. If the fluctuations are absorbed by using battery, the state of charge of the battery will swing about a given mean depth of discharge DOD_m which will be more or less equal to the average of the DODs at the peak and trough of the charge/discharge cycle. Ideally, therefore, the net energy flow into the battery would be almost zero. Fig. 2 illustrates the concept of PV fluctuation absorption in an ideal case for two different DOD_m where the mean DOD remains constant. In an actual case, the moving mean of the DOD will in time drift higher or lower due to the random nature of whether conditions.

4.1. Hysteretic control mode selection

The aim of the method developed here is to localize the cyclic charge/discharge events due to net load fluctuations to the upper band of the battery SOC regime hereafter called the smoothing band. This enables to keep the DOD_m as small as possible, reduce cycling at lower state of charge and ensure more frequent recharge all of which are favorable conditions for longer battery life. To realize such operation the hysteretic mode selection approach in Fig. 3 employing the boundaries of the smoothing band as limits is used to switch between different control modes.

The state of charge of the battery is employed as a control variable to change between the two control modes Mode 1 and Mode 2. Under Mode 1 a moving average of the fluctuating power P_{netL} is used as reference to control the power flow from/to fuel cell/electrolyzer. This enables both fuel cell and electrolyzer to operate along smooth power curves and hence the operation mode under this control mode is called smoothing. The fluctuating part of the power is then diverted to the smoothing band of the battery having center SOC set point at SOC_C, and lower and upper SOC points at SOC_L and SOC_H respectively. SOC_C can be considered as the moving mean of the peak and trough points of the SOC cycles. In principle the longest SOC cycle under Mode 1 will have a peak at SOC_H, trough at SOC_L and mean at SOC_C. A higher value of SOC_C can be achieved by choosing higher value for SOC_H and keeping the averaging period reasonably lower. The latter follows from the fact that the center SOC set point acts as DC offset about which SOC swings having amplitudes proportional to the averaging period occur.

In the event that the battery state of charge drifts outside the smoothing band, the control mode is changed to Mode 2. Mode 2 then acts to quickly return the state of charge to the SOC_C set point through bulk charging or bulk discharging the battery depending on whether the state of charge is below SOC_L or above SOC_H respectively. This is done by operating the fuel cell at full capacity during bulk charging and operating the electrolyzer at full capacity during bulk discharging to enable faster return to Mode 1. The operation mode under this control mode is therefore called bulk cycling. Once bulk cycling is started, the control mode stays in Mode 2 until the target set point SOC_C is reached. If under Mode 2 the load exceeds the combined power of the PV array and fuel cell rated capacity (or P_m is greater than the fuel cell rated power $P_{FC,R}$), i.e. under peak loading condition, the battery goes into the peaking operation mode. In peaking operation mode the control mode remains

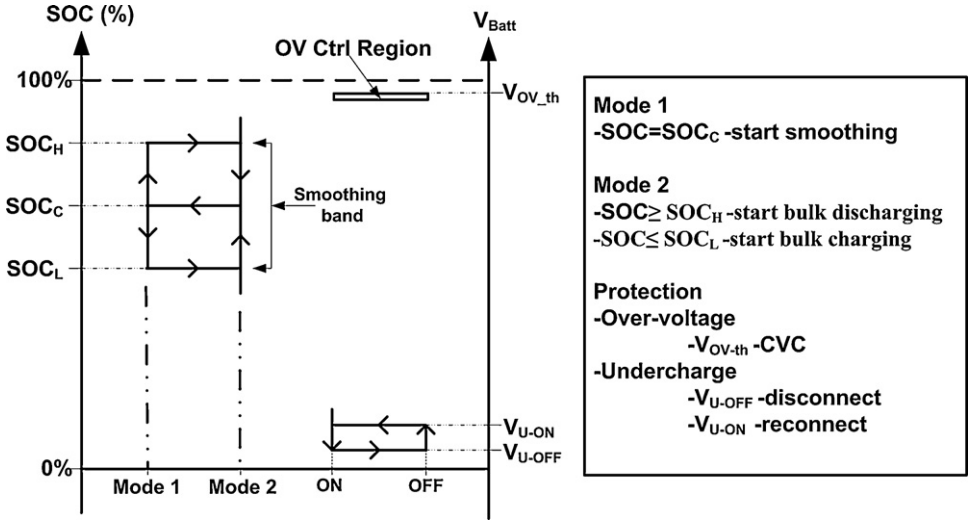

Fig. 3. Hysteretic control mode selection and protection.

Table 1
Summary of control and operation modes.

Control mode	Logical condition	Operation mode
Mode 1	$SOC = SOC_C$	Smoothing
Mode 2	$SOC < SOC_L$ OR $SOC > SOC_H$	Bulk cycling
	$SOC < SOC_L$ AND $P_m > P_{FC,R}$	Peaking

Mode 2. Even so the state of charge of the battery will continue to decrease until the peaking period passes where the battery starts bulk charging. Eventually the control mode changes to Mode 1 as soon as SOC_C is reached where smoothing operation is restarted. It should be observed that during bulk cycling both the fuel cell and electrolyzer are still operating at steady state, i.e. at rated or zero power which in effect constitutes steady state operation. On the whole, the mode switching control method should ensure battery operation within the smoothing band for most of the time of the day with intermittent operations below the band (even going as low as the minimum SOC) during peaking periods. Table 1 summarizes the control and operation modes with the respective logical conditions. A detailed representation of the transition between different operation modes at any given instant is also shown in the state machine graph in Fig. 4.

4.2. Sizing of battery and selection of the smoothing band

The battery capacity is mainly sized based on the peak power demand and how long it lasts as suppression of short term power fluctuation will require much lower capacity. The maximum kWh capacity required is thus the peak power multiplied by the peaking duration assuming a constant peak power. Variations in battery voltage with SOC change and capacity decrease with increasing discharge rate should also be taken into account. The final battery bank is then assembled as N_s cells in series depending on the voltage requirement and N_p strings in parallel depending on the current and Ah requirement.

Once the battery capacity is decided, the width and SOC_H of the smoothing band can be selected. Assuming SOC_C as the initial state of charge, the width should be selected so that the maximum charging energy will not cause the SOC to exceed SOC_H and the maximum discharge energy will not cause the SOC to go below SOC_L. SOC_H should also be sited as high as possible to prevent shifting the SOC cycles lower. Let us now consider the extreme case where the net load P_{netL} instantaneously increases from zero to a maximum $P_{\max}$ at $t = t_1$ as shown in Fig. 5. Under this condition the moving average

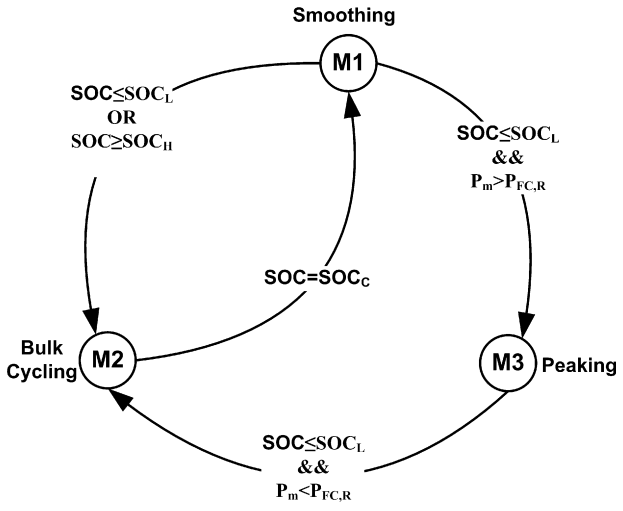

Fig. 4. State machine representation of mode transition.

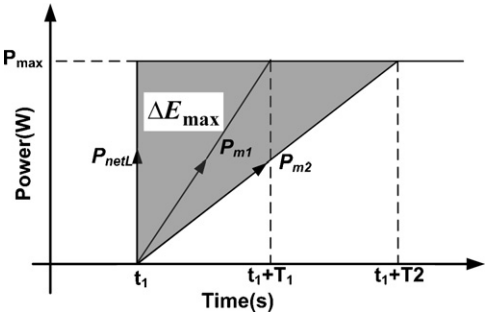

Fig. 5. Response to step change in net load.

P_m changes according to Eq. (5) while the battery power P_{batt} linearly falls from $P_{\max}$ to zero during the averaging period T following Eq. (6).

$$P_m = P_{\max}\left(\frac{t - t_1}{T}\right) \tag{5}$$

$$P_{Batt} = P_{\max}\left(\frac{T - t - t_1}{T}\right) \tag{6}$$

The battery discharges $\Delta E_{\max}$ of electrical energy given by Eq. (7) which is equivalent to the shaded area. As shown in figure the area increases with increasing averaging period, i.e. more kWh is discharged for longer averaging period. Similarly the battery charges with the same magnitude of electrical energy $\Delta E_{\max}$ for an instantaneous decrease of P_{netL} from $P_{\max}$ to zero.

$$\Delta E_{\max} = \int_{t_1}^{T+t_1} P_{Batt}\,dt = P_{\max}\left[t - \frac{t_1 t}{T} - \frac{t^2}{2T}\right]_{t_1}^{T+t_1} = \frac{1}{2}P_{\max}T \tag{7}$$

In either case $\Delta E_{\max}$ is the absolute maximum as all slower changes in P_{netL} will produce smaller areas. In reality, PV and load fluctuations occur at slower rates and are also intermittent with variations occurring within the averaging period. Although both these issues suggest the magnitude of charge/discharge energy is always less than predicted by (7), $\Delta E_{\max}$ can be used as guide line for selecting the width of the smoothing band.

Assuming an average battery voltage of V_{nom} within the smoothing band, the smoothing width Q_{smo} (in Ah) of the battery SOC regime required for the smoothing operation should comply to the relation

$$Q_{smo} \le \frac{2 \times \Delta E_{\max}}{V_{nom}} \tag{8}$$

The factor 2 is used since twice capacity is required to suppress a fast increase or decrease (by $P_{\max}$) of net load P_{netL} above or below the smooth power P_m. Substituting Eq. (7) into (8) yields

$$Q_{smo} \le \frac{P_{\max}T}{V_{nom}} \tag{9}$$

Since PV fluctuation induced battery cycling is desired to occur with as small DOD_m as possible, SOC_H is selected first with the highest possible value only leaving an allowance for over-voltage protection. SOC_C and SOC_L are then selected based on SOC_H using (10) and (11) where Q is the total battery capacity.

$$SOC_C = SOC_H - \frac{Q_{smo}}{2Q} \tag{10}$$

$$SOC_C = SOC_H - \frac{Q_{smo}}{Q} \tag{11}$$

5. Power flow control

The schematic in Fig. 6 shows how the power references for the fuel cell and electrolyzer are generated in Mode 1 using the

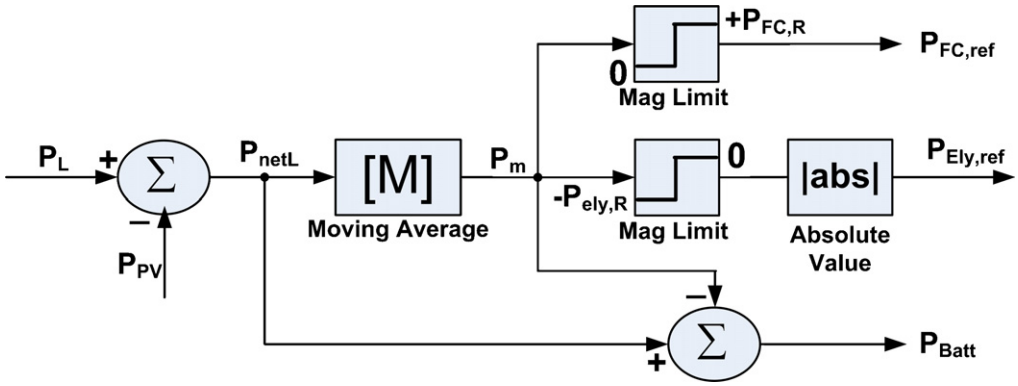

Fig. 6. Reference power generation in Mode 1.

smoothing algorithm. It can be seen that the electrolyzer and the fuel cell are not operated at the same time: depending on whether the smoothed power P_m is positive or negative either $P_{Ely,ref}$ or $P_{FC,ref}$ is respectively limited to zero effectively shutting down either one of them. The generated reference powers are used as power set points to control the respective power electronics and gas flows. In Mode 2, on the other hand, the rated powers are used as the reference set points.

Since the battery is connected to the DC-bus without using power electronics, the battery power cannot be actively controlled directly. The active control of the fuel cell and the electrolyzer powers will therefore indirectly determine the battery power. It should also be noted that as the battery is used to compensate the power losses in the various conductors and power electronic converters, any errors in the reference generation due to losses are eliminated. The actual battery power at a given instant is therefore instead

$$P_{Batt,act} = P_{nsL} - P_m + P_{losses} \tag{12}$$

where in terms of the primary losses (conversion losses in the power electronics) the total loss can be written as

$$P_{losses} = (1-\eta_{MPPT})P_{PV} + (1-\eta_{FC})P_{FC} + (1-\eta_{Ely})P_{Ely} \tag{13}$$

where η_x represents the efficiency of the respective converters.

Fig. 7 gives the overall control diagram where the control scheme is divided into two hierarchical layers: supervisory and local control.

5.1. Supervisory control

The supervisory control layer comprises the mode selection algorithm (MSA). This block receives as inputs power references generated from the smoothing algorithm, the smoothing band SOC boundaries from user, rated powers of the fuel cell and electrolyzer and the estimated (measured) state of charge of the battery. Based on the current state of charge of the battery, the MSA selects the control mode (M1 or M2) and subsequently the appropriate power set points.

In this article the state of charge variable of the battery used for the supervisory control is estimated based on the conventional charge counting method which accounts the ampere-hour loss through the ampere-hour (Ah) efficiency η_{Ah}. Although the Ah efficiency is time variant and dependent on various factors such as the battery state of charge, a constant value is used here as the aim of

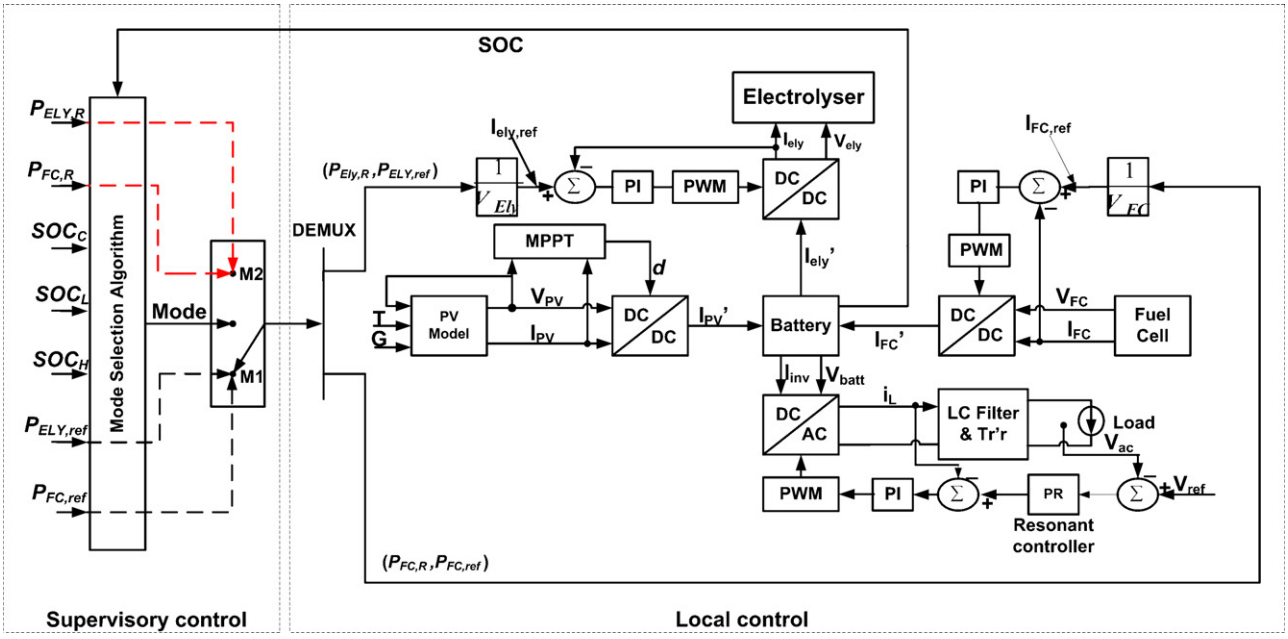

Fig. 7. Control scheme of total system.

Table 2
Parameters of studied system.

Fuel cell SS		Electrolyser SS		PV SS		VSI SS	
Fuel cell stack		Electrolyser		PV array		VSI	
V_{FC} (V)	12–20	V_{EL} (V)	20–43	V_{mpp} (V)	84.9	V_{DC} (V)	42–52
$P_{FC,R}$ (kW)	1.2	$P_{EL,R}$ (kW)	1.8	I_{mpp} (A)	46.2	V_{ac} (V_{rms})	230
I_{FC} (A)	0–100	I_{EL} (A)	0–42	V_{OC} (V)	110	f_0 (Hz)	50
FC DC/DC		EL DC/DC		I_{SC} (A)	49.8	P (kVA)	5
V_{in} (V)	12–20	V_{in} (V)	48	P_{mpp} (kWp)	3.96	N_s/N_p	11.38
$V_{out,nom}$ (V)	48 V	V_{out} (V)	20–43	DC/DC and MPPT		f_s (kHz)	50
D_{ss}	0.75	D_{ss}	0.89	$V_{in,max}$ (V)	150	L (μH)	0.3
I_{Lss} (A)	100	I_{Lss} (A)	42	$V_{out,nom}$ (V)	48	C (μF)	96
V_{Css} (V)	48	V_{Css} (V)	43	V_{th} (V)	50.5	r (Ω)	0.08
R (Ω)	0.48	R (Ω)	1.03	f_s (kHz)	20	R (Ω)	10.58
f_s (kHz)	50	f_s (kHz)	50	Update rate	1 sample	PI regulator	
L (μH)	48	L (μH)	0.4	L (μH)	330	K_P	30.27
C (μF)	52	C (μF)	30	C (μF)	50	K_I	4.65e^3
r (Ω)	0.05	r (Ω)	0.05	D_{ss}	0.57	PR controller	
H_1(s)	0.04	H_1(s) [V A^{-1}]	0.04	I_{Lss} (A)	82.5	K'_P	0.39
H_2(s)	0.167	H_2(s)	0.167	V_{Css} (V)	48	K'_I	1874.2
PI regulator		PI regulator		R (Ω)	0.58	ω_0	$2\pi f_0$
K_P	0.0508	K_P	0.0648	H_1(s) [V A^{-1}]	0.04	PM	56.1°
K_I	153.92	K_I	14.403	H_2(s)	0.167	ω_c (rad s^{-1})	7.75e^3
Lead acid battery				OV-controller			
Nom capacity (Ah)		18 × 8.0		K_p	100		
R_1 (Ω)/cell		0.0026		K_I	0.0077		
R_2 (Ω)/cell		0.0005		K'_p	0.92		
C (F)/cell		23		K'_I	318.86		

the article is mainly to demonstrate the control method developed. Accordingly the state of charge of the battery at measurement point k can be estimated as

$$SOC(k) = SOC(k-1) + \frac{\eta_{Ah} P_{Batt}(k) \Delta T}{V_{Batt}(k) Q}$$

$$= SOC(0) + \frac{\eta_{Ah} \Delta T}{Q} \sum_{i=0}^{k} \left(\frac{P_{Batt}(i)}{V_{Batt}(i)} \right) \quad (14)$$

where ΔT is the sampling time and P_{batt} is given by Eq. (12). To reduce error, the starting state of charge of the battery SOC(0) is reset at each start time by measuring the open-circuit voltage and mapping it to a corresponding state of charge using a look-up table.

5.2. Local control

The mode dependent power set point outputs of the MSA (i.e. $P_{FC,ref}$, $P_{Ely,ref}$, $P_{FC,R}$, $P_{Ely,R}$) are eventually used by the local control layer which directly controls the power flow. The external loops in the fuel cell and electrolyzer controllers use these power set points to generate the reference currents which are subsequently used by the internal current controllers to directly control the respective DC/DC converters. Due to their zero steady-state error when tracking DC quantities, Proportional-Integral (PI) controllers are used both for fuel cell and electrolyzer current control.Since the fuel cell and electrolyzer currents are actively controlled based on the state of the battery, the fuel cell and electrolyzer act as controlled current source and controlled current sink respectively. The PV subsystem, on the other hand, acts as both controlled and uncontrolled current source. This is because under normal conditions the PV array produces power at its maximum power point which is dictated by irradiance and weather conditions, and close to the battery over-voltage threshold point the PV power is controlled to limit the current going to the battery. Both MPPT and over-voltage controls used in this article are implemented using a charge controller similar to that proposed by the authors in [11] (see Appendix A for more details). An MPPT continuously seeks the operating point of a PV array at which the PV power output is maximized regardless of irradiance and temperature. If a voltage source type load is connected at the output of a DC/DC converter, the output power can be maximized by increasing the output current. The PV converter used is a buck converter to step-down the PV voltage which varies between 110 V (open circuit) and 48 V at standard conditions (see Table 2) to the battery voltage which has nominal value of 48 V. In this case since the load seen by the DC/DC converter is a battery, which is a voltage source type load as long as there is an error between the battery voltage and threshold voltage setpoint $V_{batt,ref}$ (see Appendix A), the reference current generated will increase significantly as a result of the over-voltage control action. In the controller proposed the output current will, however, never exceed the maximum current due to dynamic limitation to an upper value equal to maximum current. The maximum current is calculated using a simple MPPT algorithm based on fractional short circuit current or the fact that the maximum current is approximately linearly related to the short circuit current of the PV array and then it is referred to the battery (inductor side). The PV controller in effect is able to seamlessly change from MPPT mode to power limit mode as the battery voltage closes to the threshold value (over-voltage). On the whole, the battery voltage control objective is therefore accomplished from the DC side by injecting or sinking the required current.

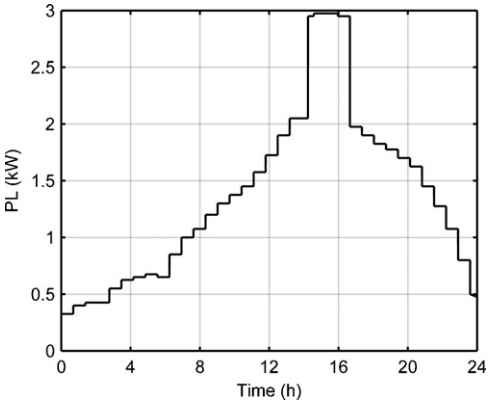

Fig. 8. Daily load curve.

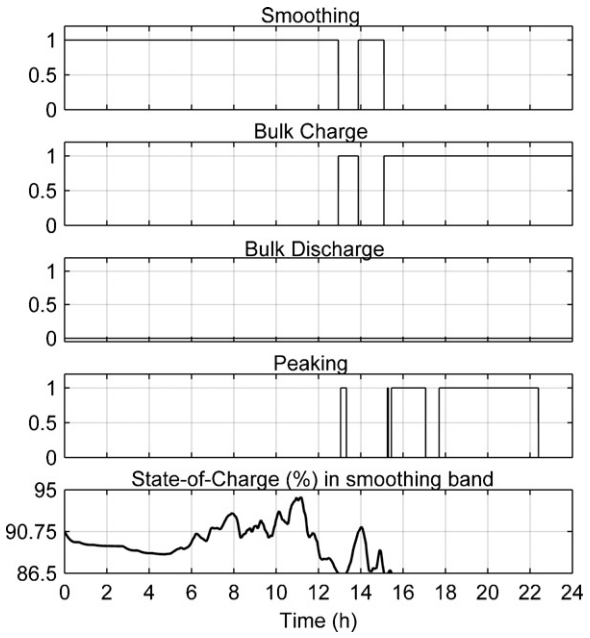

Fig. 9. Operating mode transition on April 26 [SOC_0 = 90.75].

The control objective of the voltage source inverter, on the other hand, is to produce a high quality AC voltage irrespective of variations and non-linearity in the load. Thus as long as the battery voltage is kept within the desired input range of the voltage source inverter, the required AC voltage will be maintained. Control of the inverter is realized using average current mode control (ACMC) in a dual-loop configuration with an internal current control loop cascaded with an external voltage control loop. The current control loop will enable protection of the inverter during transient faults by limiting the switch current. Having current control also ensures faster dynamic response to load and input line changes, and voltage stability due to the damping of the LC-filter poles [12]. The outer voltage control loop is realized with a proportional-resonant controller (PR) [12–14] to achieve selective compensation and zero steady-state error in the fundamental component of the voltage. The current loop is implemented using a simple PI controller as the steady state error of current is not a concern. A brief explanation of modeling of power electronics and design of the controllers used in this study is given in Appendix A. All local controllers are designed using the SISO tools in SIMULINK.

6. Results and discussion

To demonstrate the developed control method a simulation study using SIMULINK/SIMPOWER is conducted based on realistic irradiance data obtained from Oslo. The irradiance is average of 20 year data measured at 1 min resolution. The load curve given in Fig. 8 is synthesized to be able to force the various modes. All other data and parameters of the studied system including designed controller gain values are given in Table 2.

Battery capacity and smoothing band selection are done based on the data given in Table 3.

Table 3
Parameters for battery selection.

Peak load	T	P_{max}	V_{nom} (SB)	SOC_{offset}	V_{avg}
2 kW/2.4 h/day	30 min	1 kW	48 V	30%	45 V

Table 4
Simulated cases (ON = enabled, OFF = disabled).

Case	Mode changing control	Smoothing	Conventional SOC set point control
1	ON	ON	OFF
2	OFF	ON	OFF
3	OFF	OFF	ON

6.1. Battery capacity

Assuming an average battery voltage V_{avg} and constant peak load of ΔP_{peak} over a period of Δt, the usable battery capacity can be calculated as

$$Q = \frac{\Delta P_{peak} \times \Delta t}{V_{avg}} = \frac{2\,\text{kW} \times 2.4\,\text{h}}{45\,\text{V}} = \frac{4800\,\text{Wh}}{45\,\text{V}} = 106.7\,\text{Ah}$$

Gross battery capacity including the unused capacity is therefore

$$Q_{tot} = Q + 30\% = 141.6\,\text{Ah}$$

A battery stack consisting of 18 strings in parallel by 21 series sealed lead acid battery cells is therefore used. The cell data used here such as resistances and capacitance are the same as the cell studied in [15].

6.2. Smoothing band

The smoothing band is selected based on the maximum net load fluctuation, nominal battery voltage within the band and the averaging period as

$$Q_{smo} \le \frac{P_{\max} \times T}{V_{nom}} = \frac{2 \times \Delta E_{\max}}{V_{nom}} = \frac{1000\,\text{W} \times 30\,\text{min}/60\,\text{min/h}}{48\,\text{V}} = 10.4\,\text{Ah} \approx 8\%$$

Note that an averaging period of 30 min is used to allow sufficient time for both the fuel cell and electrolyzer systems to reach steady-state both thermally and in terms of power.

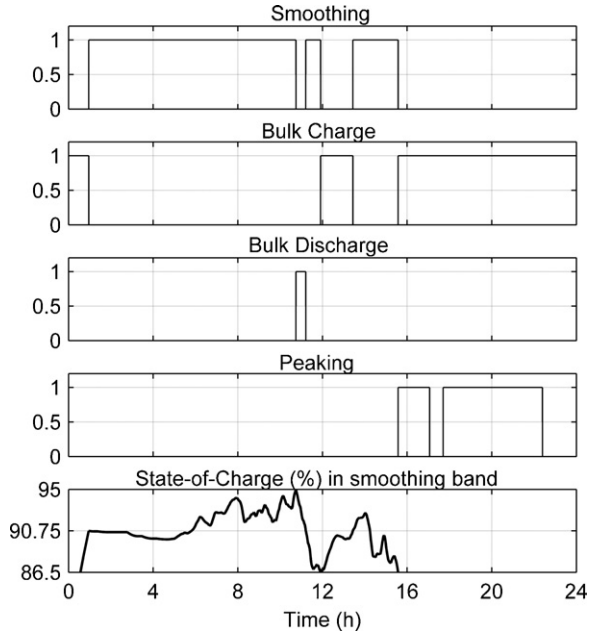

Fig. 10. Operating mode transition on April 26 [SOC_0 = 80.0].

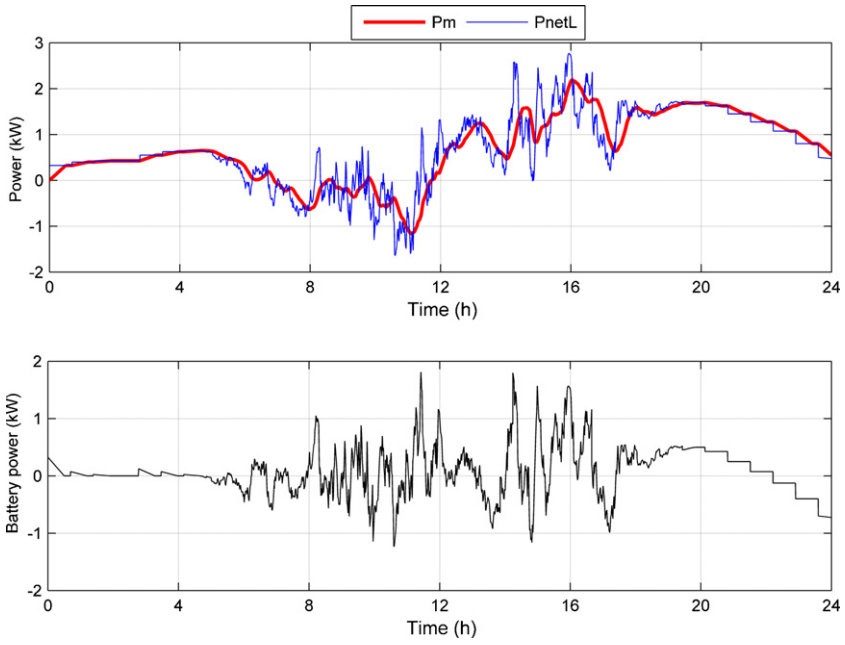

Fig. 11. Principle of diversion of power fluctuation [April 26].

Setting $SOC_H = 95\%$ first leads to $SOC_C = 95 - Q_{smo}/2 = 90.75\%$ and $SOC_L = 95 - Q_{smo} = 86.5\%$.

To help quantify the effectiveness of the developed control method, the following performance indices are defined.

6.3. Fluctuation suppression rate (FSR) [%]

This is a measure of the average level of fluctuation suppression ability as fraction of the net load. FSR is calculated during smoothing mode and is computed for fuel cell provided $P_m > 0$ and for electrolyzer provided $P_m < 0$. The FSR between the start point N_{ST} and finish point N_{FN} of the period of interest is given by (15), where $M(t_i)$ denotes the control mode at measurement point i and is 1 during smoothing mode and 0 otherwise.

$$FSR = \frac{\sum_{i=N_{ST}}^{N_{FN}} \{M(t_i) \times P_{Batt}(t_i)\}}{\sum_{i=N_{ST}}^{N_{FN}} \{M(t_i) \times P_{netL}(t_i)\}} = \frac{\sum_{i=N_{ST}}^{N_{FN}} \{M_i(t_i) \times (P_{netL}(t_i) - P_m(t_i))\}}{\sum_{i=N_{ST}}^{N_{FN}} \{M_i(t_i) \times P_{netL}(t_i)\}} \quad (15)$$

6.4. Mean SOC (MSOC) [%]

This performance index gives a measure of the time history of SOC and uses the normalized area under the SOC curve over period

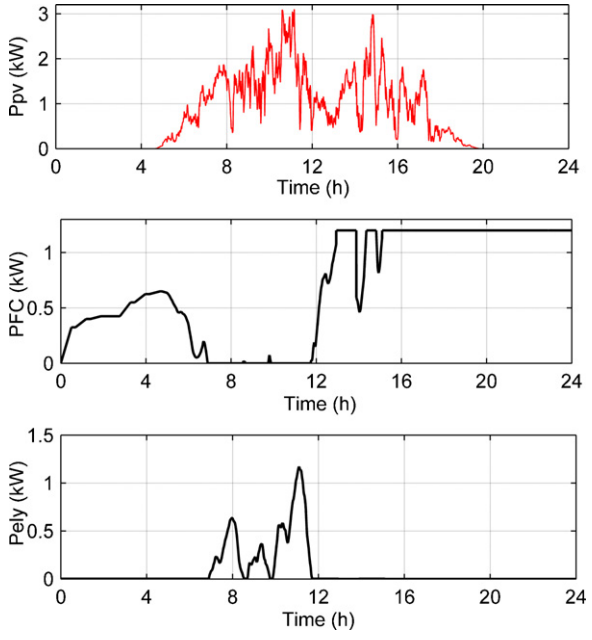

Fig. 12. PV, FC and Ely power plots on April 26 [case 1].

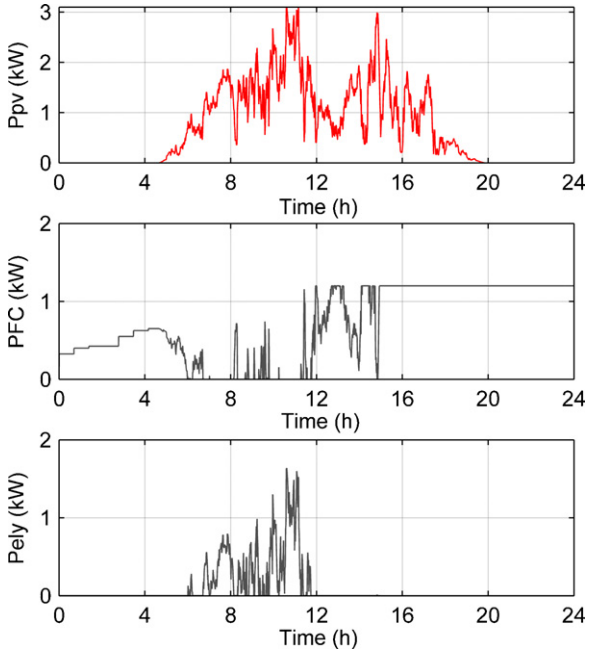

Fig. 13. PV, FC and Ely power plots on April 26 [case 3].

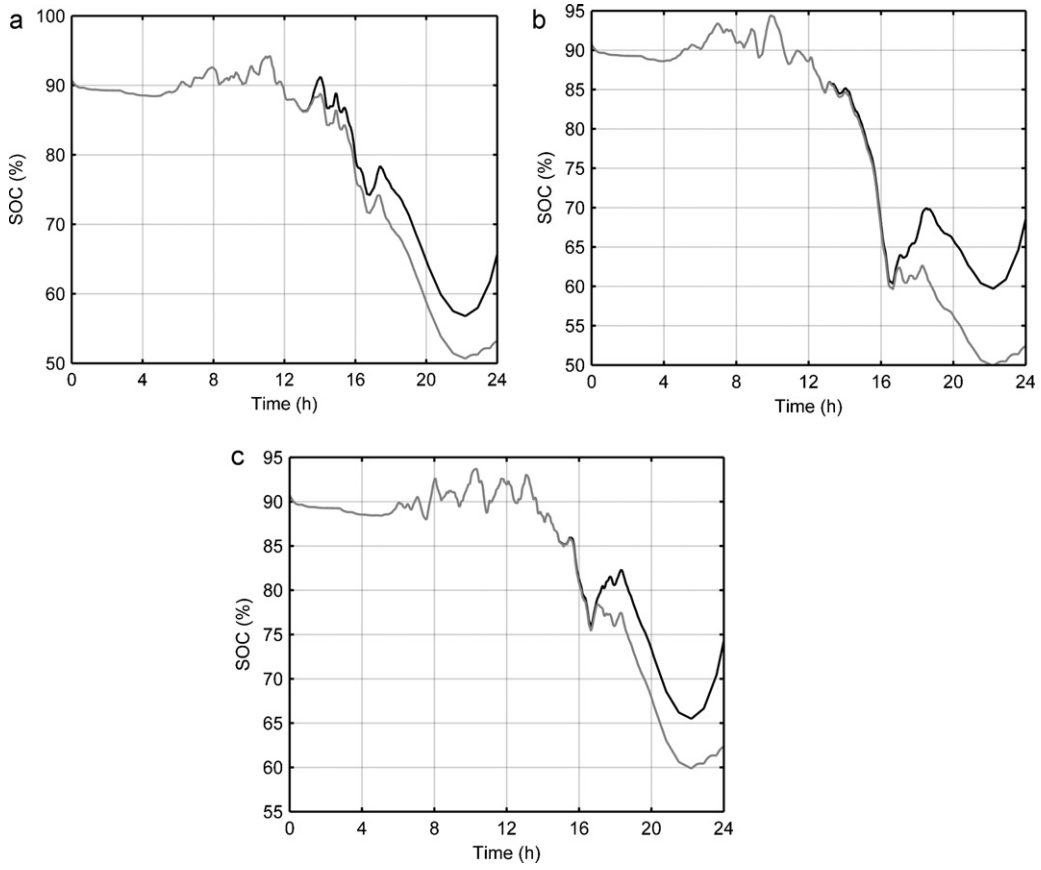

Fig. 14. (a) Time history of SOC [SOC_0 = 90.75, April 26], (b) time history of SOC [SOC_0 = 90.75, July 13] and (c) time history of SOC [SOC_0 = 90.75, August 11].

of interest as performance indicator to estimate the length of time the battery spends at a given state of charge relative to an ideally preferred state of charge (SOC_H in this case). Excluding the offset SOC, MSOC can thus computed as

$$MSOC = \frac{\sum_{i=N_{ST}+1}^{N_{FN}} \{SOC(t_i) - SOC_{offset}\} \times \Delta T}{\{SOC_H - SOC_{offset}\} \times (N_{FN} - N_{ST}) \times \Delta T} \quad (16)$$

where ΔT is the sampling period.

Three cases given in Table 4 are studied where the proposed control method (case 1) is first compared to a scenario with smoothing mode enabled but without mode changing control (case 2) and then to conventional SOC set point control (case 3). In conventional SOC set point control the battery is used only for peak shaving (and not smoothing) while the fuel cell and electrolyzer are operated in load following mode.

Results from three typical days in the summer months of April, July and August were evaluated. Figs. 9 and 10 show the operating mode transitions on April 26 as function of where the SOC of the battery lies with respect to the smoothing band when the proposed control method (case 1) is enabled. In Fig. 11 the principle of diversion of net load power fluctuations to battery using the proposed control method is illustrated. Figs. 12 and 13 give power plots of fuel cell and electrolyzer together with the available PV power on April 26 when operated under case 1 and case 2 respectively. The effect of disabling the mode changing control (case 2) compared to the proposed method (case1) is represented in the time histories of the state of charge of the battery given in Figs. 14(a)–(c) and 15(a)–(c) for two different initial SOC of battery.

Table 5 gives a summary of the performance indices obtained for all the three cases on the three days. It is observed that compared to case 2, case 1 gives higher MSOC for all the three days. This means on average a battery operated with case 1 will spend all its time at higher SOC and will have a lower weighted ampere hour (Ah) throughput for each cycle that occurs than case 2 signifying the importance of the mode changing control. The results also show that case 1 generally gives suppression rates of more than 30% and 60% of the net load for the FC and Ely respectively. Case 3, on the other hand, has negligible effect on the power fluctuations

Table 5
Performance indices for 3 typical days.

SOC (%)	Case	April 26			July 13			August 11		
		MSOC (%)	FSR		MSOC (%)	FSR		MSOC (%)	FSR	
			FC (%)	Ely (%)		FC (%)	Ely (%)		FC (%)	Ely (%)
80	1	81.47	31	84.6	79.14	29.9	73.1	85.75	39.5	89.97
	2	60.24	31	81.47	56.8	29.9	73.1	64.7	39.5	89.97
	3	79.1	5.49	0.55	78.88	6.6	0.43	84.87	5.3	0.868
90.75	1	79.8	29.5	70.58	77.4	32.2	66.75	83.41	39.05	85.9
	2	76.5	29.5	70.58	73.2	32.2	66.75	80.85	39.05	85.9
	3	79.4	5.2	0.55	79.13	6.2	0.40	85.12	5.0	0.86

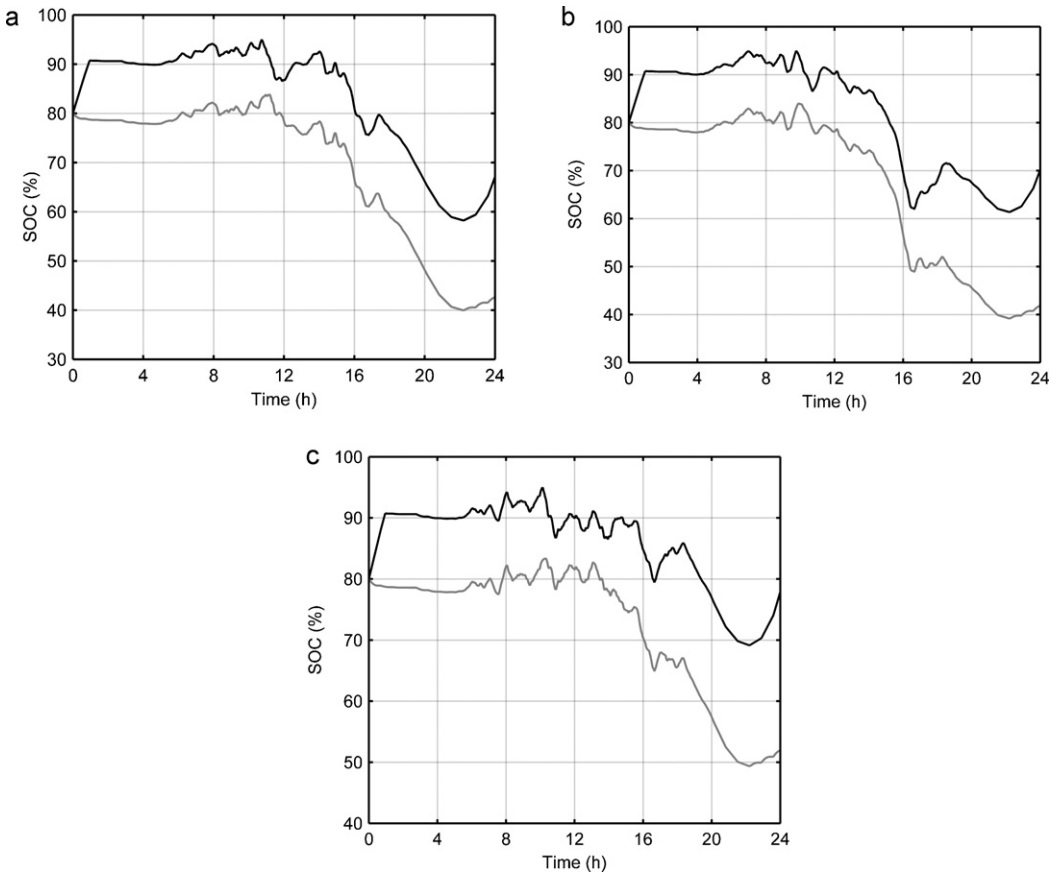

Fig. 15. Time history of SOC [SOC_0 = 80.0, April 26], (b) time history of SOC [SOC_0 = 80.0, July 13] and (c) time history of SOC [SOC_0 = 80.0, August 11].

leaving the fuel cell and electrolyzer to be operated under unstable power conditions. The results also indicate that the mode changing approach will increase the probability of frequent recharge to full charge which would be less likely without it as the battery would spend most of its time at low charge and will recharge very rarely only when excess renewable energy is available. The results for two different initial SOC show that the proposed method outperforms case 2 much better in terms of MSOC when the initial battery SOC is outside the smoothing band (80%) than when it is inside (90.75%) further consolidating the importance of the mode changing approach. MSOC values which are over 20% higher than case 2 are found for initial SOC equal to 80%. The SOC of the battery is more likely to drift outside the band after the end of each day mainly due to peaking demand.

7. Conclusions

Cost reduction is very critical in the pursuit of realizing more competitive clean and sustainable energy systems. In line with this goal a control method that enables to minimize the cost associated with performance and lifetime degradation of fuel cell and electrolyzer, and cost of battery replacement in PV–hydrogen standalone power systems is developed. The method uses the advantage of existing peak shaving battery to suppress short term PV and load fluctuations with reduced impact on the cycle life of the battery. Reduced impact on battery cycle life is achieved by localizing the diverted power fluctuations to higher band of the SOC regime. This enables to operate the fuel cell and electrolyzer under more favorable power conditions which improve performance and life time while minimizing impact on battery cycle life. In addition to performance improvement through improved system efficiency, operation under more stable power conditions improves life time of not only the FC and electrolyzer themselves but also of their balance of plants (BOPs) which will be spared off the more mechanically stressful conditions of having to work under rapidly varying loads. Simulation studies conducted demonstrate the developed method can achieve the expected results. Compared to the conventional SOC set point control, the proposed method enables significantly higher suppression rates of short term power fluctuations ensuring more stable and less abusive power operation of fuel cell and electrolyzer systems. The results also show that the mode changing approach enables to prevent lower SOC operation of battery and cycling at partial state of charge both of which may accelerate aging of lead acid batteries. The probability of frequent battery recharge is also increased with the proposed method.

Acknowledgement

This work was supported by the research council of Norway.

Appendix A.

A.1. Modeling of power electronics and controller design

In this appendix average models of power electronic converters and choice of the controllers used are briefly discussed.

A.2. Fuel cell boost converter

Averaging the on/off states of a boost converter over the switching period under continuous conduction mode (CCM) leads to the average circuit in Fig. A1 where the dashed variables represent

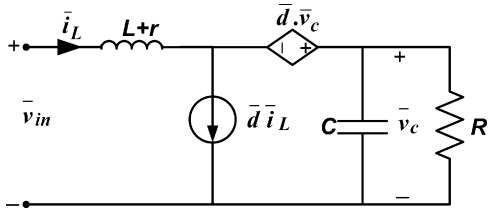

Fig. A1. Average model of a boost converter.

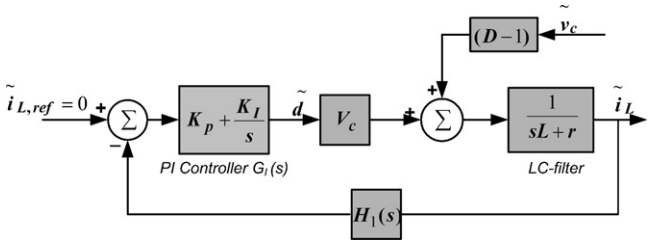

Fig. A2. Control diagram of boost converter in Laplace domain.

average values and R stands for the resistive equivalent of the load (battery in this case).

Through small signal perturbation and linearization of Kirchhoff's current and voltage equations [16] of the circuit in Fig. A1, the small signal state space average model in (A1) which can be used in control design can be written. Variables with '∼' are small signal perturbations while upper case variables correspond to steady state operating points.

$$\begin{aligned}\frac{d\tilde{i}L}{dt} &= -\frac{r}{L}\tilde{i}_L + \frac{D-1}{L}\tilde{v}_c + \frac{V_c}{L}\tilde{d}\\ \frac{d\tilde{v}_c}{dt} &= \frac{1-D}{C}\tilde{i}_L - \frac{1}{RC}\tilde{v}_C - \frac{I_L}{C}\tilde{d}\\ \tilde{v}_c &= \tilde{v}_c\end{aligned} \tag{A1}$$

After transforming (A1) into the Laplace domain, the current control diagram in Fig. A2 including the PI current regulator can be drawn. For simplicity the PWM block here is considered part of the controller gain and hence is not shown separately.

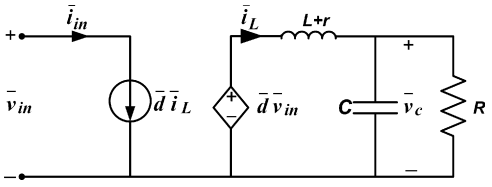

Fig. A4. Average model of a buck converter.

To design the PI controller using classical control theory, the frequency response of the open loop transfer function (TF) gain $G_{OL}=H_1G_IG_P$ where G_P is the plant transfer function given by (A2) and H_1 is the current sensor gain is analyzed.

$$G_p(S) = \frac{\tilde{i}_L}{\tilde{d}} = \frac{(V_c/L)s + (V_c + I_L(1-D)RC)/LRC}{s^2 + ((RrC + L/LRC)s + (r + (1-D)^2R)/LRC)} \tag{A2}$$

The current controller should be designed for the worst case scenario here corresponding to the minimum fuel cell voltage and full load operating condition both given in Table 2. A controller designed for these conditions via bode plots and with the gain values given in Table 2 will have a stable response with open loop cross-over frequency of $\omega_c = 2639\,\text{rad}\,\text{s}^{-1}$ and phase margin PM = 74° as shown in the bode plots in Fig. A3.

A.3. Electrolyzer buck converter

Averaging a buck converter under CCM in a similar way as previous gives the average circuit in Fig. A4. Following the same procedure as for the boost converter again yields the small signal average model given by (A3) and the current control diagram in Fig. A5 for the buck converter.

$$\begin{aligned}\frac{d\tilde{i}_L}{dt} &= -\frac{r}{L}\tilde{i}_L - \frac{\tilde{v}_c}{L} + \frac{V_{in}}{L}\tilde{d}\\ \frac{d\tilde{v}_c}{dt} &= \frac{\tilde{i}_L}{C} - \frac{1}{RC}\tilde{v}_c\\ \tilde{v}_c &= \tilde{v}_c\end{aligned} \tag{A3}$$

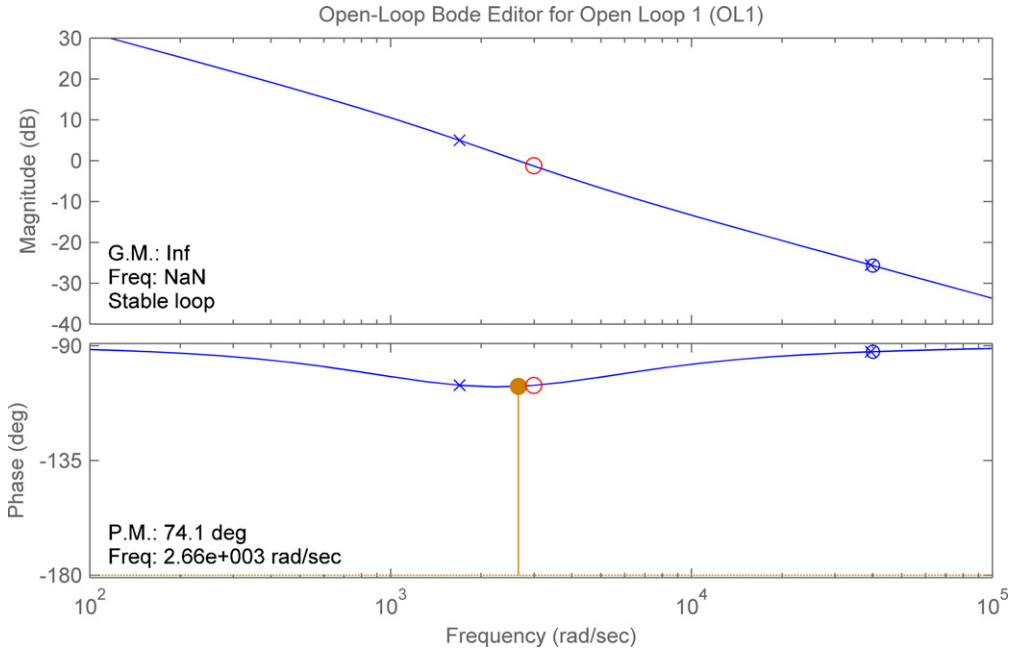

Fig. A3. Bode plot of $G_{OL}(s)$ [boost converter].

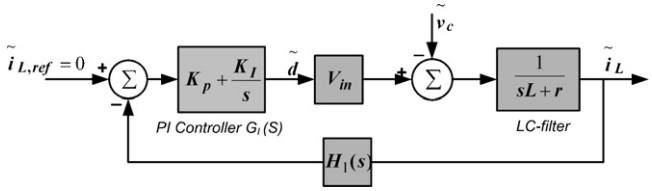

Fig. A5. Control diagram of buck converter in Laplace domain.

Following the same procedure as for the boost converter, analysis with classical control theory with the plant transfer function now given by (A4) can be applied.

The PI controller parameters selected and given in Table 2 yield stable control loop as shown in the bode plots of Fig. A6.

$$G_p(S) = \frac{\tilde{i}_L}{\tilde{d}} = \frac{V_{in}}{L} \frac{(s + 1/RC)}{s^2 + ((L + RL + RrC)/LRC)s + r(1 + R)/LRC} \quad \text{(A4)}$$

A.4. Voltage source inverter

The two legs of a single phase VSI can be assumed to be two buck converters working in opposite directions in terms of voltage. Consequently, the average equivalent of the two legs of the single phase voltage source inverter can be superposed to give the non-switching averaged model in Fig. A7 assuming bipolar pulse width modulation.

The average model has the same form as the buck converter with the only difference being the duty cycle which is now given by

$$d' = 2d - 1 \quad \text{(A5)}$$

where d is the duty cycle of the first diagonal pair of switches and d' varies sinusoidally in the range [−1,1] as d varies from 0 to 1.

The close analogy between a buck converter and VSI means that the small signal model of the VSI is similar to the small signal model of the buck converter. Fig. A8 shows a multi-loop control scheme in average current mode control (ACMC) with an external voltage control loop now added in cascade with a current control loop as the control objective is voltage control. A proportional-resonant (PR) controller is used for voltage regulation to selectively achieve zero steady-state error compensation at the fundamental frequency ω_0.

First the current controller is designed in the same manner as for the buck converter and the PI gains given in Table 2 were selected. To simplify the design of the voltage controller the closed current loop is approximated by the first order TF in (A6). The closed loop

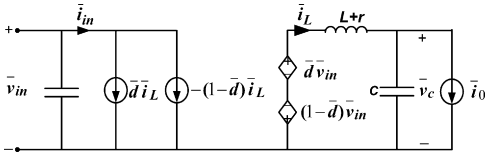

Fig. A7. Average model of single phase VSI.

gain $G_{CL}(s)$ is chosen to have a dominant time constant equal to the inverse of the cross-over frequency of the open loop TF and a gain the same as the inverse of the current transducer $H_1(s)$. The approximation will hold so long as the voltage loop is chosen to be sufficiently slower than the current loop [17].

$$G_{CL}(s) = \frac{G_o}{1 + \tau s} \quad \text{(A6)}$$

The resonant controller with parameters given in Table 2 is designed based on the simplified open voltage loop gain. Bode plots of the open voltage loop gain is shown in Fig. A9. It can be seen from the plots that the gain will have resonance at the fundamental frequency as expected which ensures zero steady-state error at the same frequency.

A.5. Battery charge controller and MPPT

A buck converter connecting the PV array to the battery acts as an active block which enables both MPP tracking and over-voltage control (details of the controller are found in [11]). The same average model of the converter as for the electrolyzer can be used with the input voltage now being V_{PV}. To derive the small signal model of the battery given in (A7) with the PV current as control input and the battery voltage as controlled state variable, the dynamic thevenin equivalent circuit model in Fig. A10 is used where $\tau = R_2xC$. All parameters used are given in Table 2.

$$G_b(s) = \frac{\tilde{v}_{Batt}(s)}{\tilde{i}(s)} = \frac{(R_1 + R_2) + R_1R_2Cs}{1 + \tau s} \quad \text{(A7)}$$

To control the battery voltage by controlling the current, two control loops are employed in a cascaded internal and external loop configuration shown in Fig. A11. Both controllers are implemented as PI (Proportional Integral) regulator. R is now the resistive equivalent of the load presented to the converter by the battery at maximum power point (MPP). Using the parameters listed in Table 2, the PI compensators C_1 and C_2 with K_p and K_I values also

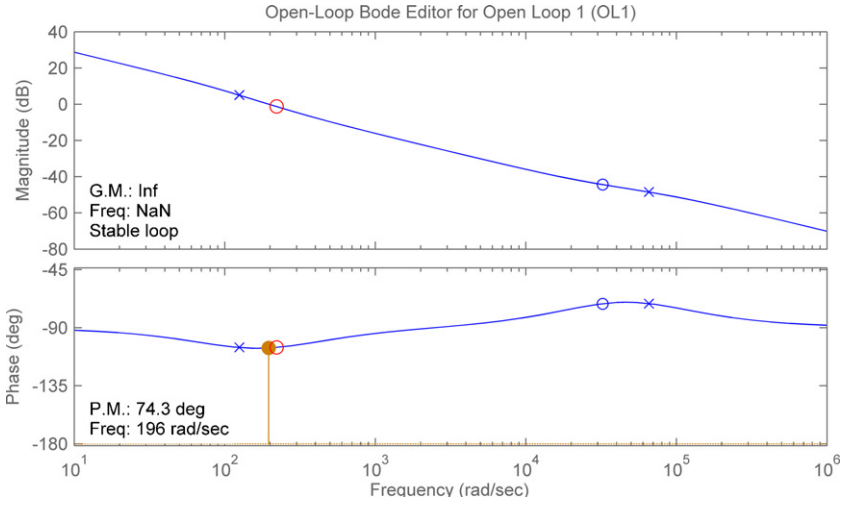

Fig. A6. Bode plot of $G_{OL}(s)$ [buck converter].

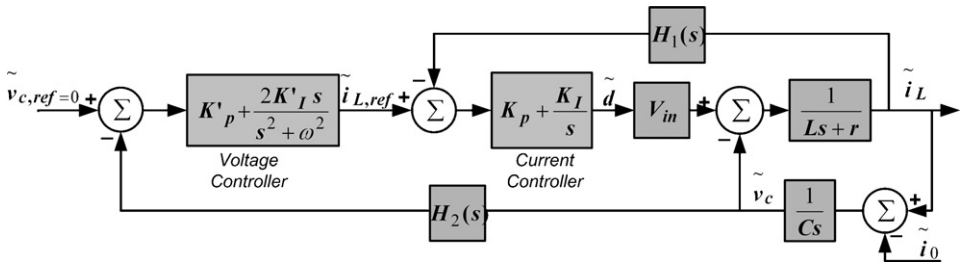

Fig. A8. Control diagram of VSI in Laplace domain.

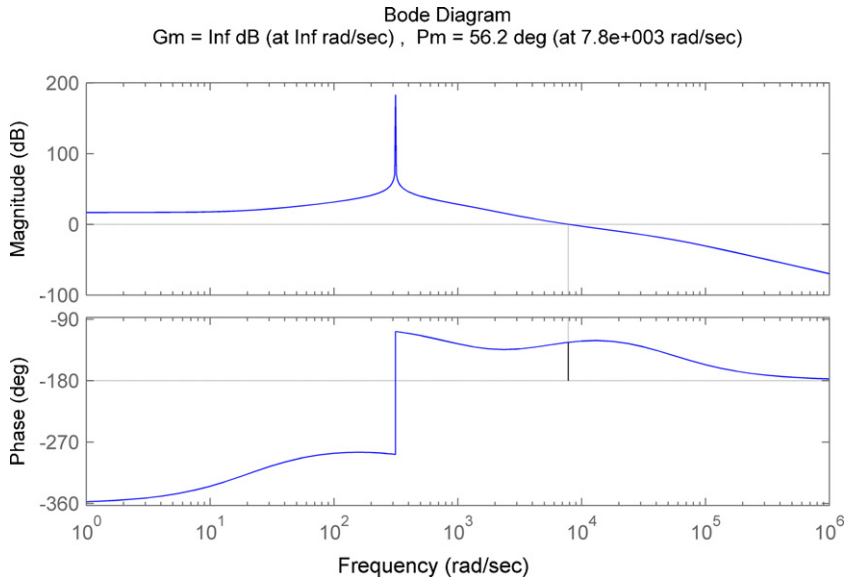

Fig. A9. Bode plot of $G_{OL}(s)$ voltage loop [VSI].

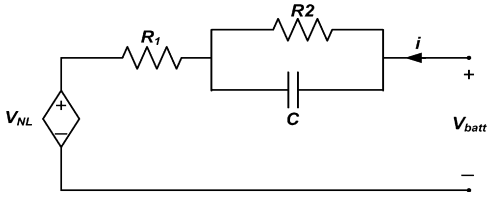

Fig. A10. Thevenin equivalent of lead acid battery.

given in Table 2 are designed to give a stable response with sufficient phase margin and band width.

Fig. A12 shows the charge controller where the current reference generated by the voltage control loop is dynamically limited to have an upper value equal to maximum power point current. This charge controller enables the PV array to always work at MPP at battery voltages away from the over voltage threshold point and the controller automatically starts shifting the PV operating point to limit the PV power produced as the voltage nears the threshold point (i.e. over-voltage control). The maximum power point current referred to the output (inductor) side of the DC/DC converter is dynamically calculated by the MPPT algorithm as a function of the instantaneous irradiance, temperature and battery voltage. This imposes a dynamic upper limit on the current going into the battery and enables a seamless change between MPPT and over-voltage control operations realized in a single control function without the need for commutation between different modes. The controller is characterized by increased PV utilization factor, high damping of voltage over-shoot and simpler and cheaper implementation owing to its single control function compared to conventional controllers.

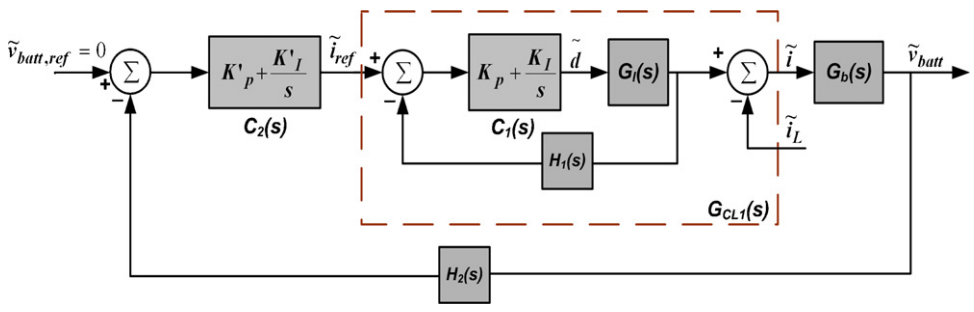

Fig. A11. Control diagram of over-voltage controller in Laplace domain.

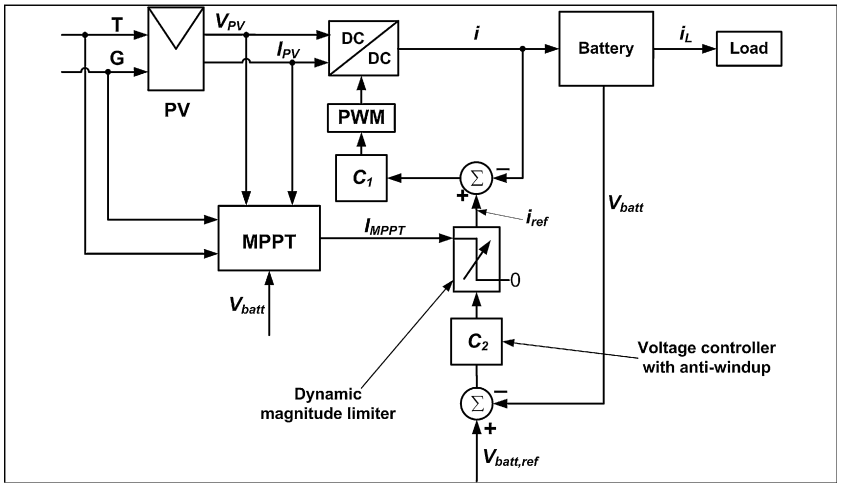

Fig. A12. Battery charge controller.

References

[1] M. Ferraro, F. Sergi, G. Brunaccini, G. Dispenza, L. Andaloro, V. Antonucci, Journal of Power Sources 193 (2009) 342–348.
[2] K. Ro, S. Rahman, Renewable Energy 13 (1998) 203–213.
[3] S.T. Lee, Z.A. Yamayee, IEEE Transactions on Power Apparatus and Systems 100 (March) (1981) 184–190.
[4] S. Yu, D. Jung, Renewable Energy 33 (2008) 2540–2548.
[5] F. Barbir, Solar Energy 78 (2005) 661–669.
[6] H. Wenzl, I.B. Gould, H. Binder, G. Bopp, 42nd Annual Conference of the Australian and New Zealand Solar Energy Society, Perth, Australia, 2004.
[7] V. Svoboda, Benchmarking – The Categorization Process, Center for Solar Energy and Hydrogen Research, Baden-Wuerttemberg, 2003.
[8] R. Kaiser, Journal of Power Sources 168 (2007) 58–65.
[9] H. Bindner, T. Cronin, P. Lundsager, J.F. Manwell, U. Abdulwahid, I. Baring-Gould, Lifetime Modelling of Lead Acid Batteries, Risø National Laboratory, Roskilde, Denmark, April 2005.
[10] J.F. Manwell, J.G. McGowan, U. Abdulwahid, a.K. Wu, Improvements to the Hybrid2 Battery Model, American Wind Energy Association Windpower 2005 Conference, May 2005.
[11] S.G. Tesfahunegn, et al., A simplified battery charge controller for safety and increased utilization in standalone PV applications, accepted for presentation at 37th IEEE PV specialist conference, Seatle, 2011.
[12] P.C Loh, D.G. Holmes, IEEE Transactions on Industry Applications 41 (2005) 644–654.
[13] N.M. AbdelRahim, et al., IEEE Transactions on Power Electronics 11 (July) (1996) 532–541.
[14] P.C. Loh, M.J. Newman, D.G. Holmes, D.N. Zmood, IEEE Transactions on Power Electronics 18 (September) (2003) 1176–1185.
[15] B.S. Bhangu, P. Bentley, D.A. Stone, C.M. Bingham, Proceedings of Vehicle Power and Propulsion Conference, 2005, pp. 780–789.
[16] Ned Mohan, Tore Marvin Undeland, Robins, Power Electronics: Converters, Applications, and Design, 3rd ed., John Wiley & Sons, Inc., 2003.
[17] S. Buso, P. Mattavelli, in: J. Hudgins (Ed.), Lectures in Power Electronics II, Morgan & Claypool, 2006.